Topographic projection of retinal ganglion cell axons at single-cell precision underlies retinotopy in the mouse superior colliculus

Authors: Dmitry Molotkov[1], Tom Boissonnet[1,2], Hiroki Asari*[1]

Affiliations:

1. Epigenetics and Neurobiology Unit, EMBL Rome, European Molecular Biology Laboratory, Monterotondo, 00015, Italy

2. Collaboration for joint PhD degree between EMBL and Université Grenoble Alpes, Grenoble Institut des Neurosciences, La Tronche, 38700, France

***Corresponding author:** Hiroki Asari, E-mail: asari@embl.it

Acknowledgments: This work was supported by research grants from EMBL (H.A.). The EMBL Genetic and Viral Engineering Facility is acknowledged for virus production; and EMBL IT Support for provision of computer and data storage servers. We thank Lin Tian (University of California Davis) for providing axon-targeted GCaMP construct; Simone Calabrese, Ilaria Sauve, Grace Cunliffe, and Matteo Tripodi for supporting experiments; and all the Asari lab members as well as Santiago Rompani for many useful discussions.

Author contributions: D.M. and H.A. designed the study; D.M. performed experiments; D.M, T.B. and H.A. analyzed the results; and D.M. and H.A. wrote the manuscript.

Competing interests: The authors declare no competing financial interests.

Abbreviated title: retinotopic RGC axon tiling in SC.

Key words: retinal ganglion cells; retinotopy; axonal imaging; superior colliculus; mouse.

Acronyms: 2D, two-dimensional; AAV, adeno-associated virus; CNMF, constrained non-negative matrix factorization; RF, receptive field; RGC, retinal ganglion cells; SC, superior colliculus; SD, standard deviation.

Abstract

Retinotopy, like all long-range projections, can arise from the axons themselves or their targets, but details of the connectivity remain unknown. Using two-photon axonal imaging, we functionally mapped the mouse retinocollicular projection at single-cell resolution. We found a near-perfect match between the spatial patterns of retinal ganglion cell axon terminals in the superior colliculus and their corresponding receptive fields, indicating that retinotopy arises from topographic axonal organizations at single-cell precision.

Main

Topographic organization is essential for the brain function (Jbabdi et al., 2013; Patel et al., 2014). Connections between brain regions are often spatially arranged to have one-to-one mappings, and sensory perception fundamentally relies on the transmission of topographically preserved information from receptor organs. In the visual system, for example, topographic visual representations are first formed in the retina and conveyed to the brain by retinal ganglion cells (RGCs) whose axons are bundled into an optic nerve (Masland, 2012). In general, neighboring RGCs project to neighboring regions in their targets (Frisén et al., 1998; McLaughlin et al., 2003; Cang and Feldheim, 2013; Arroyo and Feller, 2016). This forms a retinotopic map in the primary retinorecipient areas, such as the lateral geniculate nucleus (Malpeli and Baker, 1975) and the superior colliculus (SC; Dräger and Hubel, 1976; Cang et al., 2018), and retinotopy is likewise transferred throughout the entire visual pathways (Wandell et al., 2007; Cang and Feldheim, 2013).

How precisely is topographic information transmitted between brain regions? Only global-level relationship is known even for the best characterized connections, such as the retinal projection to SC (Frisén et al., 1998; McLaughlin et al., 2003; Cang and Feldheim, 2013; Arroyo and Feller, 2016), because such long-range projections of dense axonal fibers preclude a precise anatomical characterization of the connectivity patterns at a single-cell resolution (Hong et al., 2011). In the optic nerve, RGC axons are mixed and they lose retinotopic

organization (Figure 1; Horton et al., 1979; Colello and Guillery, 1998). A fundamental question is then if RGC axons can nevertheless find precise targets even after they get "lost" in the long-range projection (Figure 1A), or if target neurons need to reconstruct the topography by elaborating local circuitry (Figure 1B). A recent study using Neuropixel probes has demonstrated a more precise one-dimensional mapping of RGC projections to the mouse SC (Sibille et al., 2021); however, local two-dimensional (2D) organizations of RGC axon terminals remain elusive in any retinorecipient area.

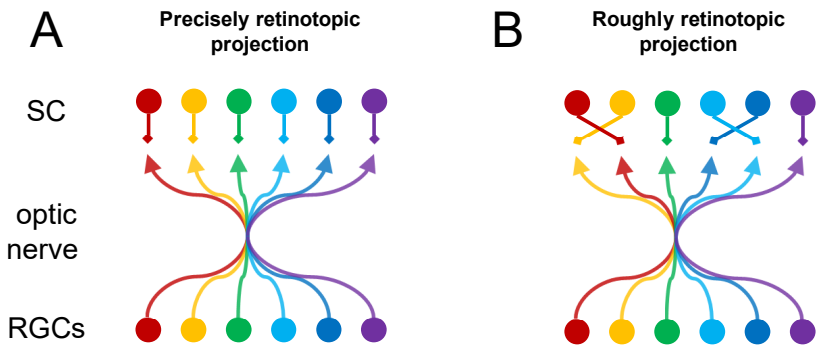

Figure 1: Possible retinocollicular projection models. Retinotopy in SC (color-coded) can arise from either (A) precisely retinotopic projection of RGC axons, innervating exact target locations in SC; or (B) roughly retinotopic projection of RGC axons while SC neurons identify appropriate partners. Note a loss of retinotopic organization in the optic nerve (Horton et al., 1979; Colello and Guillery, 1998).

To address this question, we performed functional mapping of the RGC projections to the superficial layer of SC at a single-cell resolution in awake head-fixed mice. Specifically, we expressed axon-targeted calcium indicators (GCaMP6s; Broussard et al., 2018) in RGCs via intravitreal injection of recombinant adeno-associated viruses (AAVs) harboring the pan-neuronal human synapsin (hSyn) promoter, and monitored the visual responses of the labeled RGC axons in SC using *in vivo* two-photon microscopy (Figure 2A). To segment axonal patches of individual RGCs and isolate their activity, we used constrained non-negative matrix factorization (CNMF) that allows to extract morphological and temporal features from noisy time-lapse calcium activities based on their spatiotemporal correlations (Giovannucci et al., 2019). For a field of view of approximately 0.3 mm^2 (0.57-by-0.57 mm), we detected up to 29 axonal patches displaying independent activity patterns (21 ± 5; mean ± standard deviation

(SD) here and thereafter; N = 23; e.g., Figure 2B). The size of the individual axonal patches (0.016 ± 0.008 mm^2; N = 491) is consistent with the past anatomical measurement (Hong et al., 2011), with a substantial overlap between them over the SC surface (40 ± 11 %). This supports a successful signal extraction and a good coverage of RGC axonal labelling. These data allowed us to faithfully reconstruct the local 2D map of the individual RGC axon terminals in the mouse SC (Figure 2B).

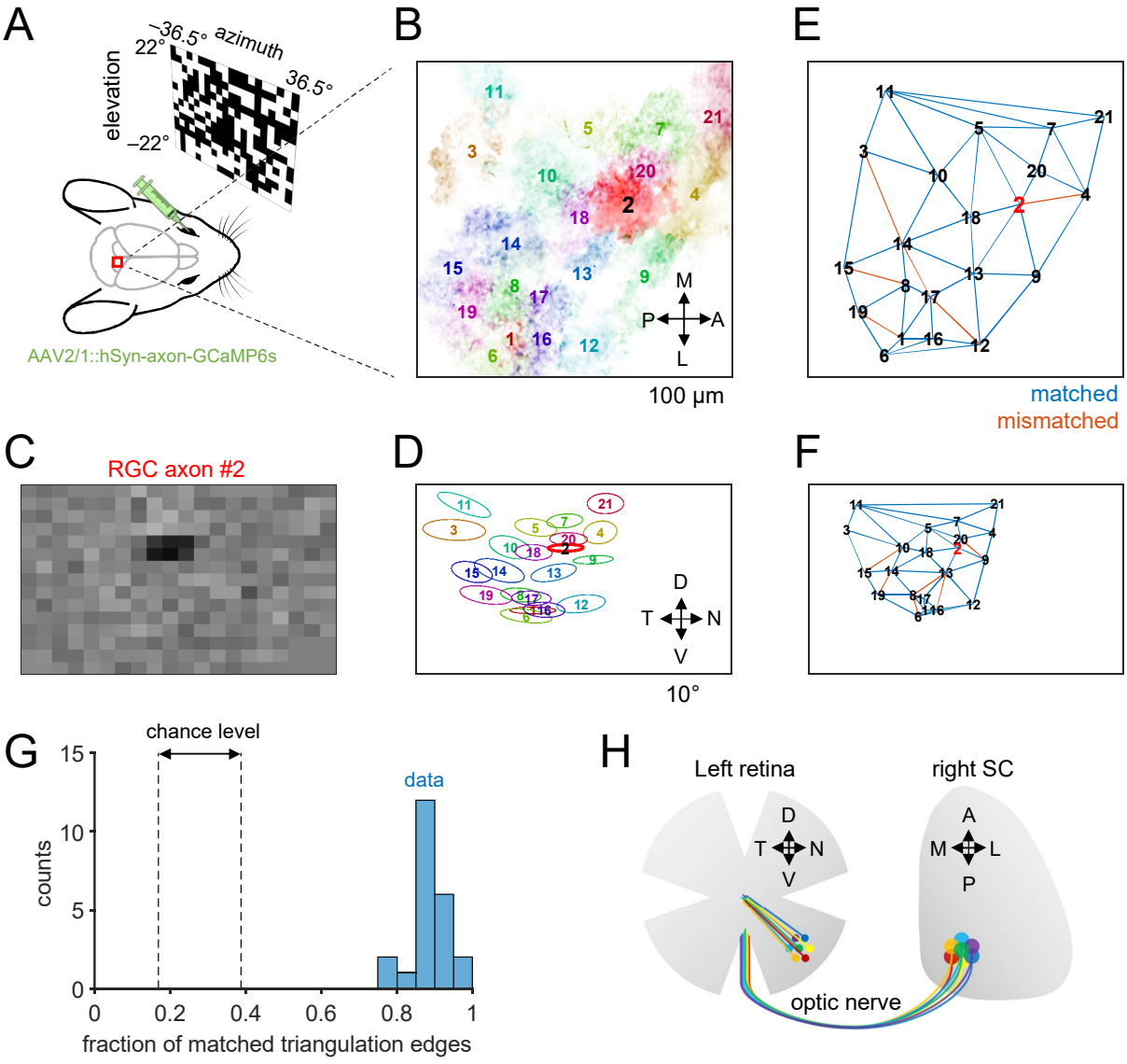

Figure 2: Retinal ganglion cell axons retinotopically tiled the mouse superior colliculus at single-cell precision. *A*: Schematic diagram of experimental set up. *B*: RGC axon patches in SC from a representative recording session. Different axon patches are shown in different colors: M-L, medial-lateral axis of the contralateral SC; P-A, posterior-anterior axis. Double-head arrows indicate the scale. *C*: Representative RF of RGC axons (#2 in B) from reverse-correlation analysis. *D*: RFs of all the simultaneously recorded RGC axons (1 SD Gaussian

profile; same color code as in B): D-V, dorsal-ventral axis of the visual field; T-N, temporal-nasal axis. *E,F*: Delaunay triangulation of the RGC axonal patch locations (E; from B) and the RF centers (F; from D): blue, matched edges between the two triangulation patterns; red, mismatched edges. *G*: Population data for the fraction of matched triangulation edges between the RGC patch locations and their RF centers (N = 23). Dotted lines indicate the chance level range at α = 0.05 (lower bound, 17%; upper bound, 39%). *H*: Summary diagram of our result, showing fine-scale retinotopic projection from the retina to SC despite a lack of retinotopy in the optic nerve (see also Figure 1A; Horton et al., 1979; Colello and Guillery, 1998).

Presence of a well-defined receptive field (RF) is a characteristic feature of all RGC types (Masland, 2012; Baden et al., 2016). To map the RF of the RGC axons, we computed the response-weighted average of the presented random checkerboard stimuli (frame rate, 4 Hz; rectangular fields 3.7° in width and 2.9° in height; “reverse-correlation”; Chichilnisky, 2001) and fitted a 2D Gaussian at the peak latency to characterize the spatial RF profile (Figure 2C,D). Most identified axonal patches had RFs within the stimulation screen (±22° in elevation and ±36.5° in azimuth from the mouse eye; Boissonnet et al., 2022). In accordance with *ex vivo* retinal physiology (Baden et al., 2016), the average RF size of the RGC axons was 6.6° ± 3.9° (N = 443), estimated as the mean of the long- and short-axis diameters of the 2D Gaussian profile at 1 SD. There was no significant correlation between the RF size and the RGC axonal patch size (Pearson's r = 0.06, p = 0.18). The RFs (1 SD Gaussian profiles) locally tiled the visual field with 9 ± 4 % overlap, where the center of every RF occupied a unique location in the visual field (Figure 2D). This ensures that these RFs belong to different RGCs because the RF center location of RGC axons should correspond well to the location of their somata in the retina – hence, the RF tiling faithfully represents retinotopy.

How well does the tiling pattern of RGC axons in SC agree with that of their RFs? As expected from the global retinotopy in SC (Dräger and Hubel, 1976; Cang et al., 2018), relative positions of the RGC axonal patches agreed well with those of the corresponding RFs (e.g., Figures 2B,D). For quantification, we used the geometric centers of the individual axonal patches and the RF center locations as landmark points in each space, and computed the Delaunay triangulation, respectively, to characterize the Euclidean adjacency relationship

regardless of their absolute positions (Figure 2E, axonal patches; Figure 2F, RF centers). Specifically, the edges of this triangulation connect all the adjacent pairs of the landmark points in a given space as a dual graph of the Voronoi tessellation that separates the space into territories close to each landmark point. We then calculated the fraction of the common edges between the two Delaunay triangulations (blue edges in Figure 2E,F) as a measure of an agreement between the two tiling patterns, and found a near-perfect match between them (88 ± 5 %; N=23; Figure 2G). This observation is consistent with the precise axonal connectivity model (Figure 1A) whereby RGC axons retinotopically tile the SC surface at single-cell precision (Figure 2H). The axon terminals of each RGC can thus innervate an exact target location despite the loss of topography in the optic nerve (Figure 1A; Horton et al., 1979; Colello and Guillery, 1998).

One of the most remarkable features of SC is a co-alignment of visual, sensory and motor maps (Cang et al., 2018). This is likely essential for sensorimotor transformation in SC, where spatial information from different sensory modalities need to be properly integrated to generate premotor outputs for visual reflexes. Given the precise retinotopy in SC (Figure 2), the other topographic maps in SC may also be organized at a fine-scale to match the spatial resolution between them.

Having a precise retinotopy facilitates spatial information processing not only at a global level, but also at local circuit levels. For example, looming detection has been suggested to arise *de novo* in the superficial layer of SC (Lee et al., 2020). In principle, this can be achieved even in the absence of retinotopy by elaborating the wiring among local neurons. It is, however, much more efficient to exploit precise topographical information because the connectivity length and its complexity can be minimized to process spatial information locally at any point in the visual field. The precise connectivity we demonstrate here suggests that the wiring efficiency indeed matters for local circuit computation.

How can then such a precise retinotopic projection be formed? The retinotopic map formation in SC occurs during the first postnatal week in mice, involving both genetic and

activity-dependent factors (Cang and Feldheim, 2013; Arroyo and Feller, 2016). These factors also play a key role in the development of a fine-scale organization in other sensory systems, such as the chemotopic map in the olfactory bulb where olfactory sensory neurons expressing the same olfactory receptor type project exclusively to the same single glomerulus (Imai et al., 2010). While overall sensory map formation is genetically predetermined by molecular cues (e.g., ephrin-Eph signaling; Frisén et al., 1998), a precise topography is established only after refinement that involves spontaneous activity, such as retinal waves during development (Arroyo and Feller, 2016), and eventually experience-driven alignment (McLaughlin et al., 2003). In particular, here we suggest that this refinement process of the retinocollicular projection should be extremely precise, to the extent that retinotopy arises at a single-cell resolution regardless of the RGC types in adult animals (Figure 2). It is then possible that neuronal circuits are in general wired more precisely than previously thought to exploit topographic information for their function, including long-range projections to other retinal targets (Liang, et al., 2018) as well as those in other systems, such as the callosal projections and entorhinal-hippocampal networks (Jbabdi et al., 2013; Patel et al., 2014).

In summary, here we performed *in vivo* functional mapping of the retinocollicular projection in awake mice and showed a precise retinotopic tiling of RGC axon terminals in SC at a single-cell resolution (Figure 2). These axons can thus innervate their exact target locations even after a loss of topographic organization through the long-range projection pathway (Figure 1A; Horton et al., 1979; Colello and Guillery, 1998). Such precise connectivity is likely beneficial for efficiently processing visual information at different spatial scales, both locally and globally. It is a future challenge to investigate the precision of the topographic organization in other brain regions, including the retinotopy in the downstream visual pathways (Wandell et al., 2007); and how precisely different topographic maps in the same brain area are aligned with each other to function coherently, such as the retinotopy, orientation, and ocular dominance maps in the mouse SC (Feinberg and Meister, 2015; de Malmazet et al., 2018).

148 # Methods

149 No statistical method was used to predetermine the sample size. All experiments involving
150 animals were performed under the license 233/2017-PR from the Italian Ministry of Health.
151 The data analyses were done in Python and MATLAB (Mathworks). All data statistics are
152 reported in the format of mean ± standard deviation (SD). The significance level was 0.05.

153 # Animals

154 A total of 10 female C57BL/6J mice were used at around 6-10 weeks of age at the time of the
155 first surgery. Mice were kept on a 12-h light / 12-h dark cycle and given water and food *ad*
156 *libitum*. After surgery, the animals were kept in groups operated on the same day. Mice were
157 between 12-24 weeks of age at the time of imaging experiments.

158 # Viral injections

159 Intravitreal injection of recombinant adeno-associated virus (AAV) chimeric serotype 1/2 was
160 used to deliver hSyn-axon-GCaMP6s expression cassette (Broussard et al., 2018) to the
161 mouse retinal ganglion cells (RGCs). For the viral injection, mice were anesthetized (induction,
162 4% isoflurane in oxygen; maintenance, 1.8-2.0%) and kept on a heated plate (Supertech
163 Physiological Temperature Controller) to avoid hypothermia. Both eyes were protected by
164 saline drop or viscous eye ointment (VitA-POS, Ursapharm). The scleral surface on the left
165 eye was exposed and a small piercing was made with a sterile 28-30G needle in between the
166 sclera and the cornea. An injection pipette (~50 μm tip diameter with 30-40° bevel) prefilled
167 with a virus solution (~1.5×10^{14} vg/mL in phosphate-buffered saline with 0.001% pluronic F68
168 and 0.001% FastGreen) was then inserted into the vitreous chamber approximately 1 mm
169 deep. The injection pipette was made from a borosilicate glass capillary (1B120F-3, WPI) with
170 a pipette puller (DMZ, Zeitz) and a microgrinder (EG-45, Narishige). After a good sealing of
171 the pipette was formed, 1.2 μL of the virus solution was injected at a rate of 10 nL/s using a
172 microinjection pump (either Neurostar NanoW or WPI NanoLiter 2010) with mineral oil (Sigma

173 M5904) filled in the displacement space by a stainless steel plunger. The pipette was slowly
174 withdrawn at least 5 minutes after the completion of the injection, and the treated eye was
175 covered with the eye ointment. The animal was then allowed to recover from anesthesia in a
176 warmed-up chamber and brought back to its home cage.

177 Cranial implantations

178 We adapted methods described in Feinberg and Meister (2015) for the cranial window
179 implantation over the mouse superior colliculus (SC). A cranial window assembly was made
180 in advance, where the surface of a circular glass coverslip (5 mm diameter, 0.13-0.15 mm
181 thickness; Assistent Karl Hecht) was activated by a laboratory corona treater (BD-20ACV
182 Electro-Technic Products) and fused to a cylindrical silicone plug (1.5 mm diameter, 0.75 mm
183 height; Kwik-Sil, WPI) by baking if for 24 hours at 70-80°C.

184 For the implantation, animals were anesthetized (induction, 4% isoflurane in oxygen;
185 maintenance, 1.5-2.0%) and placed inside a stereotaxic apparatus (Stoelting 51625).
186 Throughout the surgery, temperature was maintained at 37°C using a heated plate (Supertech
187 Physiological Temperature Controller) to avoid hypothermia, and the eyes were protected with
188 eye ointment (VitA-POS, Ursapharm). After disinfecting and removing the scalp (Betadine
189 10%, Meda Pharma), the skull surface was scratched and cleaned to ensure good cement
190 adhesion. A craniotomy of a size about 3.0 mm (anterior-posterior; AP) by 2.5 mm (medial-
191 lateral; ML) was made over the right SC using a high-speed surgical drill (OmniDrill35, WPI)
192 with a 0.4 mm ball-tip carbide bur (Meisinger). To prevent bleeding, the craniotomy was treated
193 by haemostatic sponges (Cutanplast, Mascia Brunelli) soaked with sterile cortex buffer (NaCl
194 125 mM, KCl 5 mM, Glucose 10 mM, HEPES 10 mM, $CaCl_2$ 2 mM, $MgSO_4$ 2 mM, pH 7.4).
195 The implant was then placed in a way to push the transversal sinus and posterior cortex
196 approximately 0.5 mm forward and position the silicone plug over the medial-caudal region of
197 the right SC. Tissue adhesive (Vetbond, 3M) was used to fix and seal the implant. A custom-
198 made titanium headplate (0.8 mm thick) was then cemented to the skull using acrylic cement
199 powder (Paladur, Kulzer) pre-mixed with cyanoacrylate adhesive (Loctite 401, Henkel).

After the surgery, the animal was recovered from anesthesia in a warmed-up chamber and returned to its home cage. For postoperative care, animals were given intraperitoneally 5 mg/kg Rimadyl (Zoetis) and 5 mg/kg Baytril (Bayer) daily for 3-5 days. We waited for another 10-15 days until the cranial window completely recovered before starting *in vivo* two-photon imaging sessions.

Visual stimulation

Visual stimuli were presented to the subject animals as described previously (Boissonnet et al., 2022). In short, a custom gamma-corrected digital light processing device was used to project images (1280-by-720 pixels; frame rate, 60 Hz) to a spherical screen (radius, 20 cm) placed ~20 cm to the contralateral side of an animal's eye, stimulating the visual field ±22° in elevation and ±36.5° in azimuth (Figure 2A). We presented 1) random water-wave stimuli (10 min) for generating binary masks for signal source extraction in calcium image analysis (see below); and 2) randomly flickering black-and-white checkerboard stimuli (10 min) for the receptive field mapping, with rectangular fields 3.7° in width and 2.9° in height, each modulated independently by white noise at 4 Hz.

In vivo two-photon imaging

Prior to *in vivo* imaging sessions, animals were habituated to stay head-fixed and locomote freely on a custom-made treadmill disc (8-10 habituation sessions in total over a week, each for 2 hours). For the imaging session, animals were kept on the treadmill with their head fixed for no longer than 2 hours (2-5 sessions/animal). Two-photon calcium imaging was done on a galvo-resonant multiphoton microscope (Scientifica HyperScope with SciScan image acquisition software) equipped with a mode-locked tunable laser (InSight DS+, Spectra-Physics) and a plan fluorite objective (CFI75 LWD 16X W, Nikon). In each imaging session, we performed single-plane time-lapse recordings (frame rate, 15.4 Hz) at a depth of 120-140 μm from the SC surface. The axon-GCaMP6 fluorescent signal (excitation wavelength, 920 nm; average laser power under the objective, 40-80 mW) was bandpass-filtered (BP 527/70,

Semrock) and detected with a non-descanned gallium arsenide phosphide photomultiplier tube (Hamamatsu GaAsP PMT). Each frame was acquired at 1024-by-1024 pixels (16-bit depth), corresponding to a field of view of around 0.65-by-0.65 mm.

Calcium image analysis

For preprocessing, the original images were first downsampled to 512-by-512 pixels (2-by-2 pixels averaging) to reduce noise. To correct motion artifacts, we performed 1) two iterations of Fourier-based rigid image registration in ImageJ, followed by cropping the image border by 16 pixels; and then 2) ten iterations of non-rigid motion correction (NoRMCorre) in CaImAn (Giovannucci et al., 2019), followed by a 12-pixel border crop. The resulting images (456-by-456 pixels) represent a field of view of around 0.57-by-0.57 mm (1.3 μm/pixel).

From the preprocessed images, we identified the axonal patches of individual RGCs and extracted their signals in CaImAn. Specifically, using a part of the recordings (3,000-5,000 frames representing the random water-wave stimulus presentation period), we first ran two iterations of constrained non-negative matrix factorization (CNMF) in CaImAn, where we set the number of expected components (*params.K*) to be 60 as an initialization parameter. From the identified components, we manually selected those with a uniformly-filled oval-like shape that had a size of around 50-150 μm as biologically relevant ones (Hong et al. 2011), and converted them into binary spatial masks to run two iterations of masked CNFM for processing the entire time-lapse recordings. The resulting set of spatial components (*estimates.A*) and deconvolved neural activities (*estimates.S*) was used for the subsequent analyses.

The area of the individual RGC axonal patches P_i was estimated from the identified spatial components in CaImAn (1.3 μm/pixel). The fraction of the overlap between them was calculated as the ratio of the areas between the intersection of any two patches $\bigcup_{i \neq j}(P_i \cap P_j)$ and the union of all patches $\bigcup_i P_i$.

Receptive field analysis

The receptive fields (RFs) of the RGC axon patches were estimated by reverse-correlation methods using the random checkerboard stimuli (Chichilnisky, 2001). Specifically, we calculated the response-weighted average of the stimulus waveform (0.5 s window; 1/60 s bin width), and characterized its spatial profile by the two-dimensional (2D) Gaussian curve fit at the peak latency. The RF center was assigned to the center of that 2D Gaussian profile, and the RF size was estimated as twice the mean SD of the long and short axes. The fraction of the overlap between the RFs (1 SD Gaussian profiles) was computed similarly as for the axonal patches. The Pearson correlation coefficient between the RF size and the RGC axonal patch size was calculated with the 95% interval of the data to eliminate the outliers.

Tiling data analysis

To compare the tiling patterns between the RGC axon patches and their RFs, we first computed the Delaunay triangulation of their centroid locations using the Euclidean distance in each space. As a measure of similarity between the two tiling patterns, we then calculated the number of matched edges, divided by the mean of the total number of edges in each triangulation. The chance level was calculated by a bootstrap method (10,000 repetitions).

References

Arroyo, D. A., Feller, M. B. (2016). Spatiotemporal Features of Retinal Waves Instruct the Wiring of the Visual Circuitry. Front Neural Circuits, 10, 54.

Baden, T., Berens, P., Franke, K., Rosón, M. R., Bethge, M., Euler, T. (2016). The functional diversity of retinal ganglion cells in the mouse. Nature, 529, 345-350.

Boissonnet, T., Tripodi, M., Asari, H. (2022). Awake responses suggest inefficient dense coding in the mouse retina. bioRxiv. 10.1101/2022.02.15.480512

Broussard, G. J., Liang, Y., Fridman, M., Unger, E. K., Meng, G., Xiao, X., Ji, N., Petreanu, L., Tian, L. (2018). In vivo measurement of afferent activity with axon-specific calcium imaging. Nat Neurosci, 21, 1272-1280.

Cang, J., Feldheim, D. A. (2013). Developmental mechanisms of topographic map formation and alignment. Annu Rev Neurosci, 36, 51-77.

Cang, J., Savier, E., Barchini, J., Liu, X. (2018). Visual Function, Organization, and Development of the Mouse Superior Colliculus. Annu Rev Vis Sci, 4, 239-262.

Chichilnisky, E. J. (2001). A simple white noise analysis of neuronal light responses. Network, 12, 199-213.

Colello, S. J., Guillery, R. W. (1998). The changing pattern of fibre bundles that pass through the optic chiasm of mice. Eur J Neurosci, 10, 3653-3663.

de Malmazet, D., Kühn, N. K., Farrow, K. (2018). Retinotopic Separation of Nasal and Temporal Motion Selectivity in the Mouse Superior Colliculus. Curr Biol, 28, 2961-2969.e4.

Dräger, D. C., Hubel, D. H. (1976). Topography of visual and somatosensory projections to mouse superior colliculus. J Neurophysiol, 39, 91-101.

Feinberg, E. H., Meister, M. (2015). Orientation columns in the mouse superior colliculus. Nature, 519, 229-232.

Frisén, J., Yates, P. A., McLaughlin, T., Friedman, G. C., O'Leary, D. D., Barbacid, M. (1998). Ephrin-A5 (AL-1/RAGS) is essential for proper retinal axon guidance and topographic mapping in the mammalian visual system. Neuron, 20, 235-243.

Giovannucci, A., Friedrich, J., Gunn, P., Kalfon, J., Brown, B. L., Koay, S. A., Taxidis, J., Najafi, F., Gauthier, J. L., Zhou, P., Khakh, B. S., Tank, D. W., Chklovskii, D. B., Pnevmatikakis, E. A. (2019). CaImAn an open source tool for scalable calcium imaging data analysis. eLife, 8, e38173.

297 Hong, Y. K., Kim, I.-J., Sanes, J. R. (2011). Stereotyped axonal arbors of retinal ganglion
298 cell subsets in the mouse superior colliculus. J Comp Neurol, 519, 1691-1711.

299 Horton, J. C., Greenwood, M. M., Hubel, D. H. (1979). Non-retinotopic arrangement of
300 fibres in cat optic nerve. Nature, 282, 720-722.

301 Imai, T., Sakano, H., Vosshall, L. B. (2010). Topographic mapping – the olfactory system.
302 Cold Spring Harb Perspect Biol, 2, a001776.

303 Jbabdi, S., Sotiropoulos, S. N., Behrens, T. E. (2013). The topographic connectome. Curr
304 Opin Neurobiol, 23, 207-215.

305 Lee, K. H., Tran, A., Turan, Z., Meister, M. (2020). The sifting of visual information in the
306 superior colliculus. eLife, 9, e50678.

307 Liang, L., Fratzl, A., Goldey, G., Ramesh, R. N., Sugden, A. U., Morgan, J. L., Chen, C.,
308 Andermann, M. L. (2018). A Fine-Scale Functional Logic to Convergence from Retina to
309 Thalamus. Cell, 173, 1343-1355.e24.

310 Malpeli, J. G., Baker, F. H. (1975). The representation of the visual field in the lateral
311 geniculate nucleus of Macaca mulatta. J Comp Neurol, 161, 569-594.

312 Masland, R. (2012). The Neuronal Organization of the Retina. Neuron, 76, 266-280.

313 McLaughlin, T., Torborg, C. L., Feller, M. B., O'Leary, D. D. (2003). Retinotopic map
314 refinement requires spontaneous retinal waves during a brief critical period of development.
315 Neuron, 40, 1147-1160.

316 Patel, G. H., Michael, D. K., Snyder, L. H. (2014) Topographic organization in the brain:
317 Searching for general principles. Trends Cogn Sci, 18, 351-363.

318 Sibille, J., Gehr, C., Benichov, J. I., Balasubramanian, H., Teh, K. L., Lupashina, T.,
319 Vallentin, D., Kremkow, J. (2021). Strong and specific connections between retinal axon

mosaics and midbrain neurons revealed by large scale paired recordings. bioRxiv. 10.1101/2021.09.09.459396

Wandell, B. A., Dumoulin, S. O., Brewer, A. A. (2007). Visual field maps in human cortex. Neuron, 56, 366-383.